# **Supporting Information**

## Candelli et al. 10.1073/pnas.1307824111

#### SI Materials and Methods

Preparation of DNA Constructs for Optical Tweezers Experiments. Preparation of DNA templates suitable for generating ssDNA in optical tweezers experiments was described previously (1). Briefly, to produce a 38.4-kbp construct having biotin labels on the ends of the same strand, we started our reaction by digesting phage lambda dsDNA (0.25 mg/mL) with FastDigest ApaI (30 min at 37 °C). This reaction yielded two different products, a 10.1-kbp and a 38.4-kbp dsDNA. Afterward, in the same tube, we added Klenow buffer (final concentration 0.28x), nucleotides (dGTP, dTTP; final concentration 0.067 mM), biotin-modified nucleotides (biotin-14-dATP and biotin-14-dCTP; final concentration 0.043 mM), and Klenow DNA polymerase exo- (final concentration 0.07 U/µL). The polymerization was carried out at 37 °C for 30 min. The reaction was heat inactivated (10 min at 75 °C) and ethanol precipitated. The pellet was resuspended in 50  $\mu$ L of 10 mM Tris, pH 7.5. The second part of the protocol consisted of the annealing of a primer containing four biotin-dTTPs (incubation 15 min at 65 °C; primer sequence: 5'-cTcTcTcTctcttccttctcttggcc 3'; final concentrations, 1 µM; capital letters indicate biotin positions). The hybridized primer was ligated with T4 DNA ligase (45 min at room temperature; T4 DNA ligase final concentration: 1  $U/\mu L$ ). The reaction was heat inactivated (5 min at 65 °C) and ethanol precipitated.

To produce a 48.5-kbp dsDNA construct for generating ssDNA by force-induced melting, lambda phage DNA was biotinylated at the 3' and 5' ends of the same strand by using three oligonucleotides. First, the 5' end of lambda DNA and oligonucleotides 1 (5'- ggg cgg cga cct gga caa-3') and 2 (5'- agg tcg ccg ccc ttt ttt tTt TtT-3') were phosphorylated for 30 min at 37 °C in a reaction containing 14 nM lambda DNA or 10 µM of the oligonucleotide and 0.25 U/µL of T4 polynucleotide kinase in 1× T4 ligase buffer (Fermentas). Next, oligonucleotides 1 and 3 (5'- TtT tTt ttt ttt aga gta ctg tac gat cta gca tca atc ttg tcc-3') were annealed to the overhangs of lambda DNA in a 10:1 oligonucleotide:DNA ratio (total volume 500 μL) by heating the reaction to 65 °C and cooling slowly to room temperature. The ligation reaction then was initiated by adding T4 DNA ligase (0.02 U/µL) and carried out for 2 h. Next, oligonucleotide 2 was annealed in a 100:1 ratio to the lambda DNA construct by incubation at 45 °C for 30 min. Subsequently, the oligonucleotide was ligated to the DNA at room temperature. Finally, the DNA was purified by ethanol precipitation.

**Experimental Conditions.** Microsphere catching, DNA tethering, RAD51-recombinase incubation, and fluorescence imaging were performed in the following conditions (unless otherwise mentioned): 25 mM Tris, pH 7.5; 100 mM KCl; 1 mM CaCl<sub>2</sub>; 0.5 mM ATP; and 10 mM DTT. DNA overstretching and melting were performed in 10 mM Tris, pH 7.5; 25 mM KCl; 1 mM CaCl<sub>2</sub>; 0.5 mM ATP; and 10 mM DTT.

Combined Optical Tweezers, Fluorescence Microscopy, and Microfluidics Setup. The experimental setup was described in detail elsewhere. In brief, our combined dual optical trapping and single-molecule fluorescence setup is built around an inverted microscope (Nikon Eclipse TE2000-U). Optical traps are generated by a powerful near-IR laser (Ventus 1064 nm, 3 W; Laser Quantum). An optical isolator (Newport 1030–1080 ISO-FRDY-OPT) is placed directly in front of the laser output to prevent coupling of back-reflections into the laser cavity. A combination of a zero-order half-wave plate (WPH10M-1064; Thorlabs) and a polarizing beam splitter

(10BC16PC.9; Newport) is used as a power regulator. A second zero-order half-wave plate (WPH10M-1064; Thorlabs) and polarizing beam splitter (10BC16PC.9; Newport) are used to set the linear polarization and split the laser into two independent beams. After the laser is split, a Galilean telescope (1:2.67) is used to obtain the desired beam diameter (~8 mm) and to steer the trap position. In one path, computer-controlled steering is achieved by displacing the first telescope lens with motorized actuators (T-LA28; Zaber Technologies Inc.). The two beams are recombined by using a second polarizing beam splitter (10BC16PC.9; Newport) and coupled into a high-N.A. water-immersion objective (PlanApo 60x, N.A. 1.2; Nikon) via a dichroic mirror (950 dcsp; Chroma Tech Corp.). The focusing power of the objective produces a 3D optical trap in which individual beads may be trapped and manipulated. Force detection is achieved by collecting the transmitted trapping light via a high-N.A. oil-immersion condenser (Achromat/Aplanat, N.A. 1.4; Nikon) and imaged on a positionsensitive diode (DL100-7PCBA3; Pacific Silicon Sensor) using a single achromatic lens. The unwanted polarization is rejected by a polarizing beam splitter (10BC16PC.9; Newport).

The end-to-end distance of the DNA is monitored by acquiring bright-field images of the trapped beads. The sample is illuminated by a blue light-emitting diode (LXHL-NB98 Luxeon Star/O; Lumileds), a single lens, and a dichroic mirror, and images are recorded with a CCD camera (CCD-902K; Watec) and digitized by a frame grabber.

Fluorescence excitation is performed using a wide-field strategy. Alexa Fluor 555 is excited by a 532-nm laser (GCL-0.25L, 25 mW; CrystaLaser). The fluorescence excitation beam first is expanded and then coupled into the microscope via a dichroic mirror (z532rdc; Chroma Technology Corp.) and a lens. The emitted fluorescence signal is passed through a band-pass filter (hq575/50m; Chroma Technology Corp.), imaged on an EMCCD camera (Cascade 512B; Princeton Instruments), and read by using the Winview software.

A glass, custom-fabricated, multichannel laminar flow system is used to obtain parallel flow and to exchange buffer rapidly during the experiment. Image analysis is performed using a custom-written program in LabVIEW (National Instruments).

The setup combining optical trapping, confocal microscopy, and microfluidics was described in detail in a recent publication (2).

#### **Stochastic Modeling of Filament Formation**

To test the hypothesis that RAD51 filament formation on DNA does not require standard binding cooperativity and/or a finite nucleation cluster, here we set up a minimal model without such cooperativity but with equilibrium preformation of oligomers in solution. The model we propose, which is schematically represented in Fig. S84, is completely determined by the physical properties of individual RAD51 monomers.

Monomer-Monomer (Un)binding and the Equilibrium Distribution of Oligomers in Solution. We first seek to explain our observation that the solution contains a mix of oligomeric species that can bind DNA by considering association and dissociation constants between individual monomers. In equilibrium, oligomers are continuously formed and broken up according to the law of mass action. When we assume that the oligomers have a linear, filamentous form, we can write  $K_{\rm d}^{\rm f-f}(n,m)[{\rm RAD51}_{n+m}]=[{\rm RAD51}_n]$  [RAD51<sub>m</sub>], with  $K_{\rm d}^{\rm f-f}(n,m)$  being the disassociation constant between ends of linear oligomers. The simplest model is one in which the dissociation constant between oligomers is independent of filament lengths  $K_{\rm d}^{\rm f-f}(n,m)=K_{\rm d}^{\rm f-f}(1,1)=K_{\rm d}^{\rm m-m}$ .

The resulting distribution of oligomer lengths is exponential  $[RAD51_n] = K_d^{m-m} ([RAD51_1]/K_d^{m-m})^n$ . We can further express the concentrations of the various sizes of linear structures in terms of the overall protein concentration  $[RAD51] = \sum_{n=1}^{\infty} n[RAD51_n]$ :

$$[RAD51_n] = K_d^{m-m} \exp[-n\epsilon_{sol}/k_BT],$$

$$\begin{aligned} \epsilon_{\text{sol}} \left( K_{\text{d}}^{\text{m-m}}, [\text{RAD51}] \right) \\ &= -k_{\text{B}} T \ln \left( 1 + \frac{K_{\text{d}}^{\text{m-m}}}{2[\text{RAD51}]} - \sqrt{\frac{K_{\text{d}}^{\text{m-m}}}{[\text{RAD51}]}} \sqrt{1 + \frac{K_{\text{d}}^{\text{m-m}}}{4[\text{RAD51}]}} \right). \end{aligned} \tag{S1}$$

Here,  $\epsilon_{\rm sol}$  may be interpreted as the free energy cost per monomer to form a linear oligomeric structure, and is completely determined by the total protein concentration and the monomer-to-monomer dissociation constant.

Oligomer–DNA Binding Dynamics in the Low-Coverage Regime. As the total coverage of RAD51 on the DNA molecule remains very low throughout the experiments, we may safely ignore the possibility of existing oligomers blocking the binding of other filaments. Under this condition, the time evolution of p(n,t), the probability that a position contains the left end of a linear oligomer of length n at time t, satisfies

$$\frac{\partial p(n,t)}{\partial t} = -k_{\text{off}}^{\text{f-D}}(n)p(n,t) + k_{\text{on}}^{\text{f-D}}(n)[\text{RAD51}_n],$$

$$n \ge 1, \quad p(n,t) \ll 1.$$

Here,  $k_{\rm off}^{\rm f-D}(n)$  is the rate at which an oligomer of length n dissociates from the DNA strand, and  $k_{\rm on}^{\rm f-D}(n)[{\rm RAD51}_n]$  is the rate at which the oligomers bind from solution to DNA. With the initial condition p(n,0)=0, we have

$$\begin{split} p(n,t) &= \frac{[\text{RAD51}_n]}{K_{\text{d}}^{\text{f-D}}(n)} \left(1 - e^{-tk_{\text{off}}^{\text{f-D}}(n)}\right), \\ K_{\text{d}}^{\text{f-D}}(n) &= \frac{k_{\text{off}}^{\text{f-D}}(n)}{k_{\text{d}}^{\text{f-D}}(n)} \ll [\text{RAD51}_n], \quad n \geq 1. \end{split}$$

Keeping to the simplest possible explanation, we now take the onrates of oligomers to be directly proportional to the linear oligomer concentration in the buffer as described above, i.e.,  $k_{\rm on}^{\rm f-D}(n)=k_{\rm on}^{\rm m-D}$ . Although this ignores geometric effects induced by oligomer length (e.g., the increase of the effective interaction distance with oligomer size), such effects are expected to have a much weaker influence on binding rates than does the modeled exponential decay of the linear oligomer concentration. We further assume that each monomer in a DNA-bound filament independently interacts with the DNA, and each contributes a fixed amount  $\epsilon_{\rm DNA}$  to the dissociation barrier  $k_{\rm off}^{\rm f-D}(n)=k_{\rm off}^{\rm m-D}\exp(-(n-1)\epsilon_{\rm DNA}/k_{\rm B}T)$ . The dynamics of our model system now are determined completely in terms of the total protein concentration [RAD51], the monomer-to-monomer dissociation constant  $K_{\rm off}^{\rm m-m}$ , the monomer-to-DNA dissociation constant  $K_{\rm off}^{\rm m-D}$ , the monomer off-rate from DNA  $k_{\rm off}^{\rm m-D}$ , and the permonomer increase in the dissociation barrier  $\epsilon_{\rm DNA}$ . The full distribution may be expressed as

$$\begin{split} p(n,t) &= \frac{K_{\rm d}^{\rm m-m} \exp[-\epsilon_{\rm sol}/k_{\rm B}T]}{K_{\rm d}^{\rm m-D}} e^{-(n-1)(\epsilon_{\rm sol}-\epsilon_{\rm DNA})/k_{\rm B}T} \\ &\times \left(1 - e^{-tk_{\rm off}^{\rm m-D} \exp(-(n-1)\epsilon_{\rm DNA}/k_{\rm B}T)}\right), \end{split}$$

where it should be remembered that  $\epsilon_{sol}$  is completely determined by  $K_d^{m-m}$  and [RAD51].

**Apparent Minimal Filament Nucleation Cluster.** For any given time t, the maximum filament length on the DNA that has had time to equilibrate with the buffer is  $n^*(t) \approx 1 + (k_{\rm B}T/\epsilon_{\rm DNA})\ln(t~k_{\rm off}^{\rm m-D})$ . For filaments with  $n \ll n^*(t)$ , we thus have the equilibrated distribution

$$p(n,t) \propto e^{(n-1)(\epsilon_{\text{DNA}} - \epsilon_{\text{sol}})/k_{\text{B}}T}, \quad n \ll n^*(t).$$

If times and filament lengths are such that  $n \gg n^*(t)$ , filaments that have attached to the DNA have not yet had time to fall off, and the occupation probability grows linearly with time and in proportion to the distribution of the length of the linear oligomeric structures in the buffer:

$$p(n,t) \propto t e^{-n \epsilon_{\text{sol}}/k_{\text{B}}T}, \quad n \gg n^*(t).$$

From this, it is clear that if  $\epsilon_{\rm DNA} > \epsilon_{\rm sol} > 0$ , then the filament length distribution on the DNA is peaked around  $n^*(t)$ . Interestingly, upon observing filaments at incubation time  $t_{\rm inc}$ , one might be tempted to conclude that filaments predominantly nucleate at lengths longer than  $n^*(t_{\rm inc})$ .

### **Maximum-Likelihood Fitting**

Here we describe how we fit our proposed model to the data using maximum-likelihood estimation, yielding estimates for both model parameters and their confidence intervals (through bootstrapping).

**Fluorophore Distribution.** The number of attached fluorophores f attached to each monomer is not uniform but distributed according to some probability function  $q_1(f)$ . The observed number of fluorophores f in a fiber of n monomers then is distributed according to

$$q_n(f) = \sum_{f_1, \dots, f_n=0}^{\infty} q_1(f_1)q_1(f_2)\dots q_1(f_m)\delta_{f, \sum_{m=0}^n f_m} = (q_1^*)^n(f).$$

Here,  $\delta$  is the Kronecker delta function and  $(q_1^*)^n$  is the *n*-fold convolution over the total number of fluorophores. The probability of finding f flourophores attached (through a filament) to a binding position is given by

$$P(f,t) = \sum_{n=1}^{\infty} q_n(f)p(n,t).$$

In our system, the only nonzero fluorophore probabilities are  $q_1(1) = 3/4$  and  $q_1(2) = 1/4$ , and the above expression gives a direct link between the observed distribution of fluorophores P(f,t) and the underlying distribution of oligomers p(n,t).

**Fitting the Fluorophore Distribution.** Our fits are generated by maximizing the likelihood of the observed fluorescence of the DNA molecules, given our model parameters  $\theta = \{k_{\rm on}^{\rm m-D}, k_{\rm off}^{\rm m-D}, \epsilon_{\rm sol}, \epsilon_{\rm DNA}\}$ . This amounts to minimizing the function

$$L\left(\theta, \left\{N_f\right\}_{f=0}^{\infty}\right) = -\ln\prod_{f=0}^{\infty} P(f, t_{\text{inc}}|\theta)^{N_f} = -\sum_{f=0}^{\infty} N_f \ln P(f, t_{\text{inc}}|\theta)$$

with respect to the parameter set  $\theta$ . In the above,  $t_{\rm inc}$  is the experimentally set incubation time and  $N_f$  is the number of filaments observed with f flourophores. The total number of binding sites observed without any filament binding is given by  $N_0 \approx N_{\rm DNA}N_{\rm exp}$ , where  $N_{\rm DNA}$  is the number of binding sites per tether and  $N_{\rm exp}$  is the number of experiments. To estimate the

model parameters, we numerically minimize L, and to estimate the error in the fit parameters, we perform the fit on 1,000 bootstrapped datasets. We report the best fit of the original data together with the SD in the fit parameters as calculated over the bootstrapped dataset:

$$k_{\text{on}}^{\text{m-D}} = 10^{-5.9 \pm 0.8} / \text{nM} \cdot \text{s}, \quad k_{\text{off}}^{\text{m-D}} = 10^{1.5 \pm 0.8} / \text{s},$$

$$\epsilon_{\text{sol}} = (1.1 \pm 0.3) k_{\text{B}} T$$
,  $\epsilon_{\text{DNA}} = (1.8 \pm 0.5) k_{\text{B}} T$ .

Using the fact that the experiments were performed at [RAD51] = 12.5 nM, the above may be translated to

$$K_{\rm d}^{\rm m-D} = 10^{1.4 \pm 1.1} \text{ mM} \approx 25 \text{ mM},$$

$$K_{\rm d}^{\rm m-m} = 10^{1.2 \pm 0.26} \text{ nM} \approx 17 \text{ nM},$$

$$k_{\rm off}^{\rm m-D} = 10^{1.5 \pm 0.8} / \rm s \approx 32/s, \quad \epsilon_{\rm DNA} = (1.8 \pm 0.5) k_{\rm B} T.$$

The fit of our model to the measured dataset is presented in Fig. S8B for the nucleus-size distribution of Fig. 1D, obtained after  $t_{\rm inc}=77$  s incubation and subsequent interrogation with wide-field fluorescence microscopy. The set of parameters obtained from these fits indicates that the average RAD51 oligomer size in solution (not bound to DNA) was  $n_{\rm sol}=1/(1-e^{-\epsilon_{\rm sol}/k_{\rm B}T})\approx 1.5$  monomers.

**Nucleation Rates and Cooperativity.** *Apparent nucleation rate.* Because an experiment detects only filaments that are bound at the end of the incubation time, it will report only on an effective binding rate. The measured apparent filament-binding rate is given by

$$k_{\rm on}^{\rm app} \approx 3.7 \cdot 10^{-7} / {\rm s}.$$

This should be compared with the actual filament-binding rate inferred from our fits:

$$k_{\rm on} = k_{\rm on}^{\rm m-D} \sum_{n=1}^{\infty} [{\rm RAD51}_n] = \frac{k_{\rm on}^{\rm m-D} K_{\rm d}^{\rm m-m}}{e^{\epsilon_{\rm sol}/k_{\rm B}T} - 1} \approx 1.1 \cdot 10^{-5}/{\rm s}.$$

 Candelli A, et al. (2013) A toolbox for generating single-stranded DNA in optical tweezers experiments. Biopolymers 99(9):611–620. At 12.5 nM RAD51, we thus estimate that the true binding rate  $k_{\rm on}$  is about 30 times larger than the apparent binding rate  $k_{\rm on}^{\rm on}$  reported on in Fig. 1C, predicting that only 1 in 30 of the filaments that bind to the DNA still remains attached at the end of the incubation time. The real-time measurements reported in Fig. S4 indeed confirm that a very substantial fraction of small nuclei binds to ssDNA for times shorter than the incubation times used in our wide-field experiments (Fig. 1). Using the same parameter values as fitted from the wide-field experiments ( $t_{\rm inc}$  = 77 s) above (Fig. S8B), the model quantitatively predicts (Fig. S8C) the nucleus-size distribution obtained from the better time-resolution confocal fluorescence experiments ( $t_{\rm inc}$  = 3 s; Fig. S4C).

Apparent binding cooperativity. As the amount of binding cooperativity usually is inferred from the exponent  $n_{\rm PL}$  of a power-law fit of on-rates as a function of concentration, it is of interest to examine how  $k_{\rm on}^{\rm app}$  depends on [RAD51]. Because we are working in the low-coverage regime, well before any saturation effects become important, we normally would expect cooperative binding to obey

$$k_{\text{on}} \propto [\text{RAD51}]^{n_{\text{PL}}} \Rightarrow n_{\text{PL}} = \frac{d \ln k_{\text{on}}}{d \ln [\text{RAD51}]}$$

Here, an exponent of the power-law fit  $n_{\rm PL} > 1$  usually is taken to indicate cooperative binding in clusters of size  $n_{\rm PL}$ . Following this, we define the concentration-dependent apparent exponent of the power-law fit as

$$n_{\rm PL}^{\rm app} = \frac{d \ln k_{\rm on}^{\rm app}}{d \ln [{\rm RAD51}]},$$

which corresponds to the local slope in a log-log diagram of the apparent binding rate vs. concentration.

With our estimates for microscopic parameters, the apparent exponent of the power-law fit in the concentration range around [RAD51] = 12.5 nM is  $n_{PL}^{app} = 2.0$ . The average apparent exponent in the concentration range used in our experiment (7.5 nM to 75 nM) is 1.6, in good agreement with the experimentally measured value.

Heller I, et al. (2013) STED nanoscopy combined with optical tweezers reveals protein dynamics on densely covered DNA. Nat Methods 10(9):910–916.

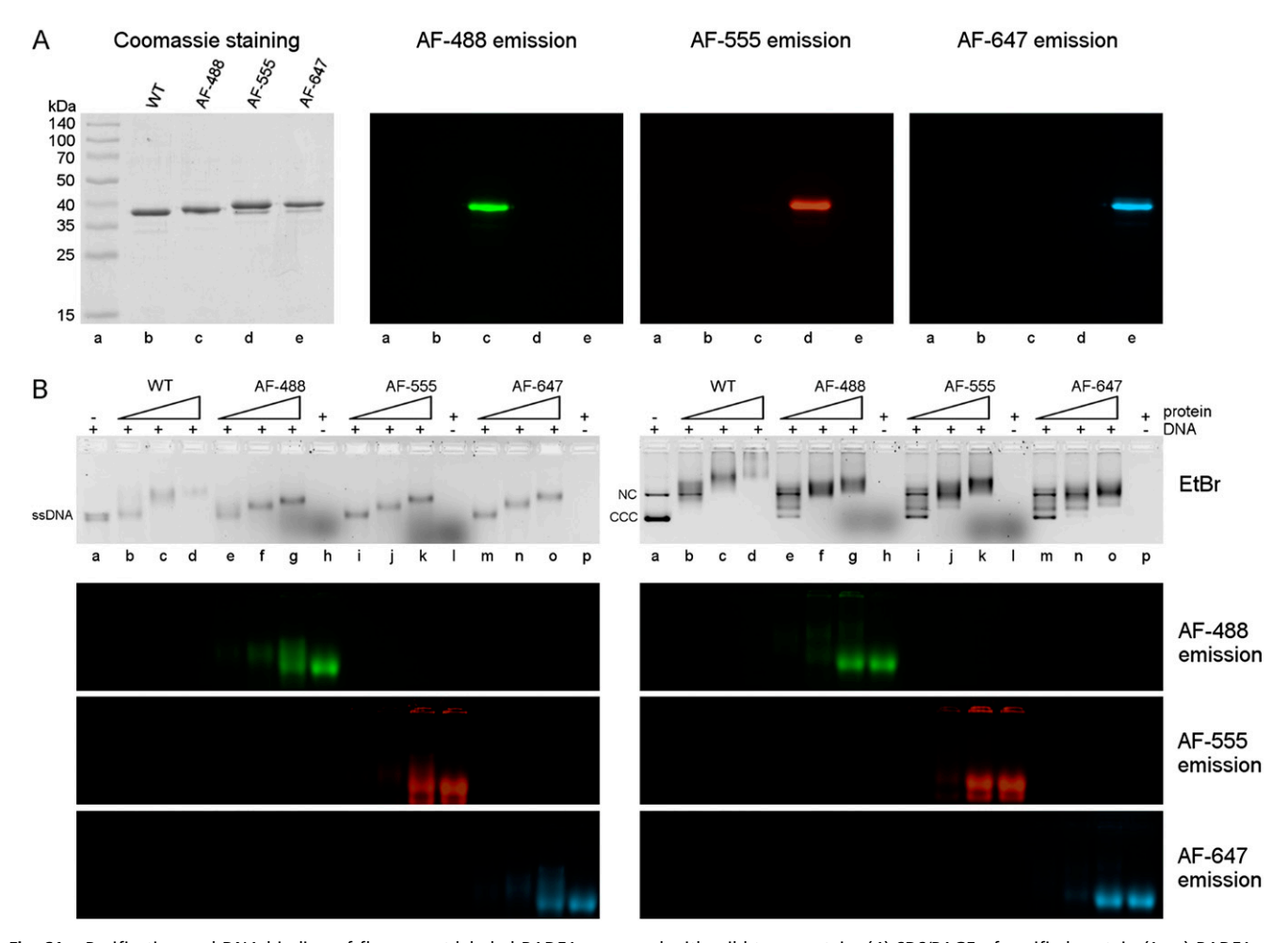


Fig. S1. Purification and DNA binding of fluorescent-labeled RAD51 compared with wild-type protein. (*A*) SDS/PAGE of purified protein (1 μg) RAD51 unlabeled wild-type (lane b), RAD51 C319S labeled with Alexa Fluor 488 (lane c), RAD51 C319S labeled with Alexa Fluor 555 (lane d), and RAD51 C319S labeled with Alexa Fluor 647 (lane e). After electrophoresis, the gel was analyzed with the ChemiDoc MP Imaging System (BioRad; Image Lab 4.1 software) to specifically excite and detect emission of Alexa Fluor 488, Alexa Fluor 555, and Alexa Fluor 647, respectively. Next, the gel was stained with Coomassie Brilliant Blue R-250 to reveal all proteins and visualized by bright-field illumination (leftmost image). Lane a, molecular weight standard. (*B*) Electrophoretic mobility shift assay showing that the covalent attachment of Alexa Fluor dyes to RAD51 cysteine 31 does not interfere with its single-stranded (*Left*) or double-stranded (*Right*) DNA-binding activity. Each protein was incubated with ssDNA (PhiX174 virion ssDNA) or dsDNA (PhiX174 replication form I dsDNA) (200 ng) in a 20-μL reaction volume containing 75 mM KCl; 55 mM Tris-HCl, pH 7.5; 0.5 mM EDTA; 0.25 mM DTT; 2.5% (vol/vol) glycerol; 1 mM ATP; and 2 mM CaCl<sub>2</sub> and increasing amounts of protein (0.5 μM, 1 μM, 2.5 μM). After 30-min incubation at 37 °C, the binding reactions were analyzed by electrophoresis in a 0.8% agarose/Trisborate gel without EDTA. The gel first was scanned with the ChemiDoc MP Imaging System (BioRad; Image Lab 4.1 software) to detect Alexa-labeled RAD51 proteins (*Lower Left* and *Right*). Next, the gel was stained with ethidium bromide (EtBr) to detect DNA (*Upper*). Lanes: a, DNA alone; b–d, unlabeled wild-type RAD51; e–h, RAD51 C319S labeled with Alexa Fluor 647; h, l, and p, labeled RAD51 at 2.5 μM without DNA. AF, Alexa Fluor; CCC, covalently closed circles; NC, nicked circles.

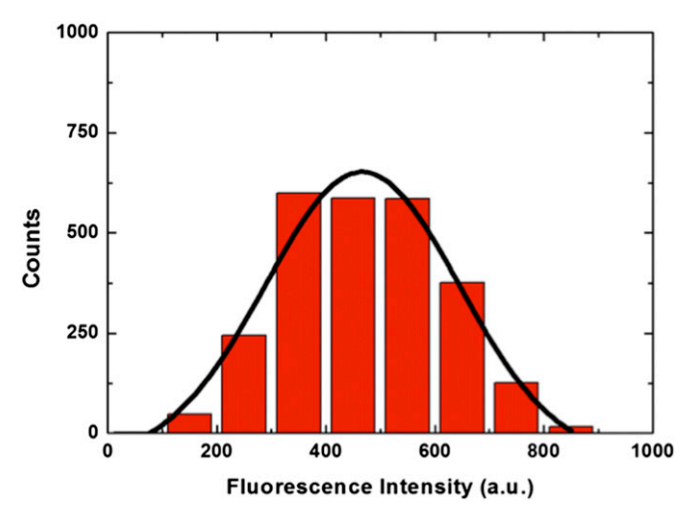


Fig. S2. Fluorescence single-molecule calibration histogram. The histogram shows the values of the fluorescence intensity trace of the single steps of multiple photobleaching traces (n = 20). Black line represents a Gaussian fit (Xc = 460,  $\sigma = 160$ ). The low-intensity variation allows quantification of the number of fluorophores contained in each fluorescent spot. Photobleaching traces are recorded during fluorescence movies of RAD51 nucleoprotein on ssDNA held between optical tweezers.

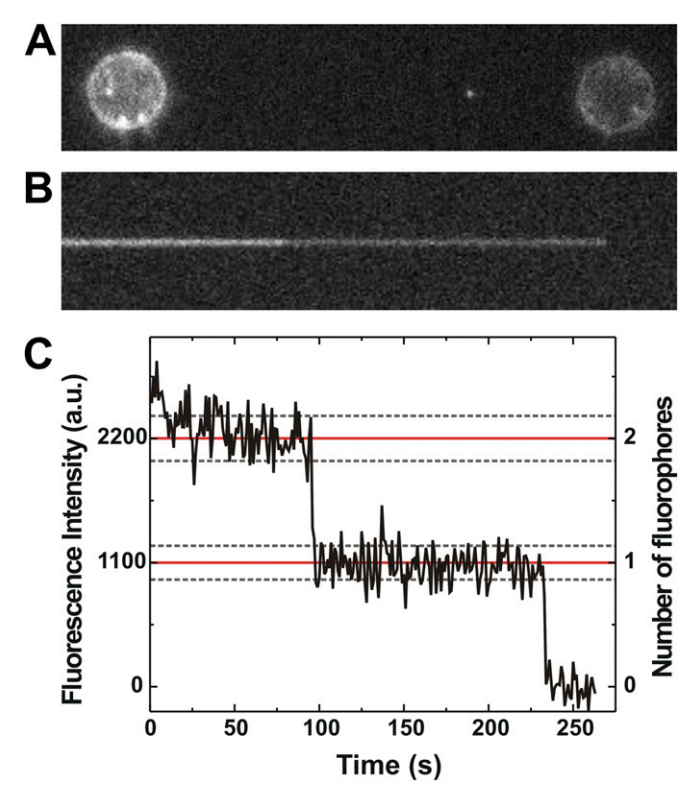


Fig. 53. Detection of dimeric RAD51 nucleus on ssDNA. (A) Fluorescent snapshot of an individual ssDNA molecule kept at 40 pN after a 77-s incubation in the enzyme channel containing 12.5 nM RAD51. An individual fluorescent spot was detected. (B) Kymograph representation of the fluorescence bleaching trace. (C) Fluorescence intensity shows a distinct staircase pattern. Two bleaching events can be recognized easily and allow quantification of RAD51 within the nucleus. In this experiment, we set the camera exposure to 1,000 ms and increased the laser excitation for obtaining high signal to noise. The presence of two steps in the photobleaching trace indicates that the RAD51 nucleus was composed of two monomers, each labeled with one Alexa Fluor 555 dye. Alternatively, it is possible that we observed the presence of a single RAD51 monomer labeled with two Alexa Fluor 555 dyes. Photobleaching traces of RAD51 nuclei on ssDNA were used to calibrate the fluorescence intensity of a single Alexa Fluor 555 dye, as reported in the main text.

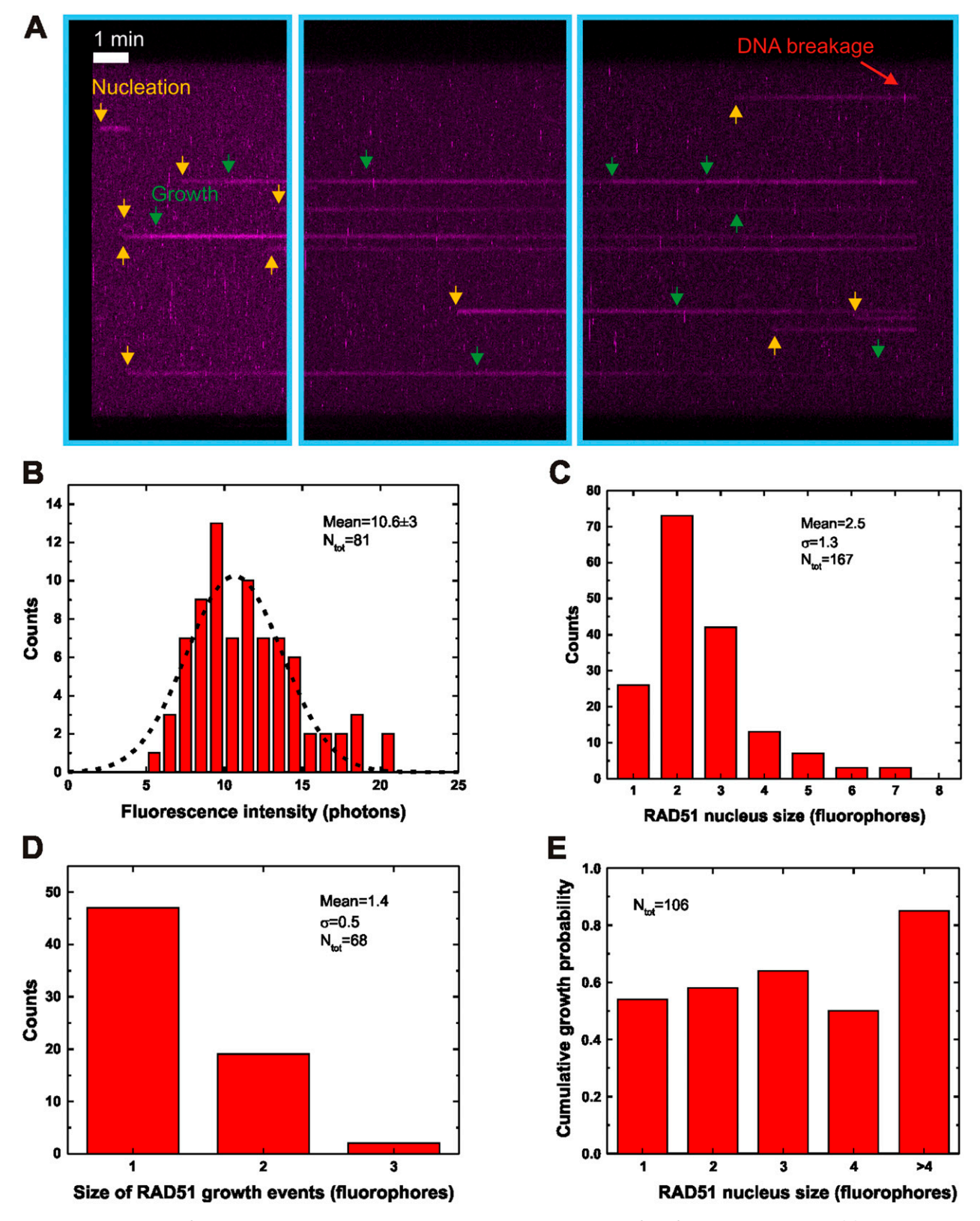


Fig. S4. Real-time detection of dynamic RAD51 binding on optically stretched ssDNA by using confocal fluorescence microscopy. (A) Kymograph showing RAD51–Alexa Fluor 555 binding dynamics on ssDNA (48,502 nt, force = 20 pN) at 25 nM of RAD51 in solution. Imaging was performed by scanning 100-nm pixels with a 2-ms dwell time along a line, with a line-scanning rate of 1 Hz. Lines on the kymograph represent binding–unbinding events of RAD51 species of different sizes, illustrating that nucleation (yellow arrows) by preformed oligomeric species of RAD51 of different sizes (fluorescence intensities) occurs in a single step from solution. Individual growth events of RAD51 nuclei also are observed in this experiment, indicated by green arrows. (B) Calibration of single-fluorophore intensity was performed by analyzing the intensities of single photobleaching steps (n = 81). (C) Size distribution of the nucleation events shows a heterogeneous distribution of sizes, ranging from single monomers to larger multimeric species. Note that unlike the wide-field measurements presented in Legend continued on following page

Fig. 1, these data are real time, also showing short, transient binding events, and allow direct discrimination of nucleation and growth. (*D*) Histogram of the number of fluorophores involved in RAD51 growth events. (*E*) Histogram of the cumulative probability that a nucleus (of given size) experiences growth after nucleation, during the whole time it was observed. Twelve of 24 nuclei consisting of one fluorophore were observed to grow, as were 24 of 41 two-fluorophore nuclei, 18 of 28 three-fluorophore nuclei, 4 of 8 four-fluorophore nuclei, and 6 of 7 nuclei with more than four fluorophores. Data show that nuclei containing four or more fluorophores (so multiple RAD51 proteins) are as proficient in growing as smaller species.

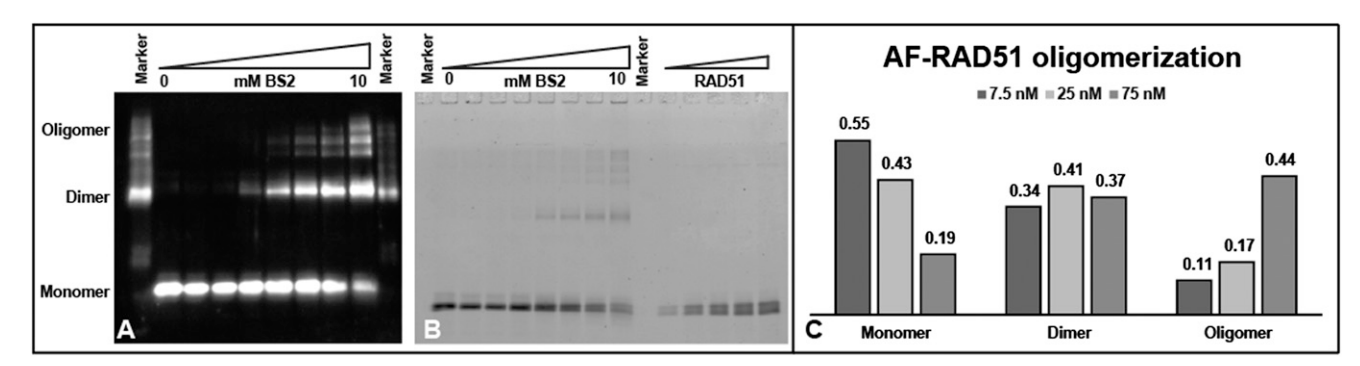


Fig. S5. Alexa Fluor 555–RAD51 cross-linking in solution with Bis(sulfosuccinimidyl) glutarate (BS2). Cross-linked complexes were resolved by polyacrylamide gel electrophoresis. Detection of Alexa Fluor 555–RAD51 by anti-RAD51 Western blot (A) and typhoon scan of the Alexa Fluor 555 fluorescence signal (B) show that with increasing cross-linker concentration, more defined multimeric species of RAD51 are cross-linked. The example shows cross-linking at 75 nM RAD51. (C) The fractions of the different forms of RAD51 determined from densitometry scanning of protein cross-linked at 7.5 nM, 25 nM, and 75 nM RAD51 and run on SDS/PAGE.

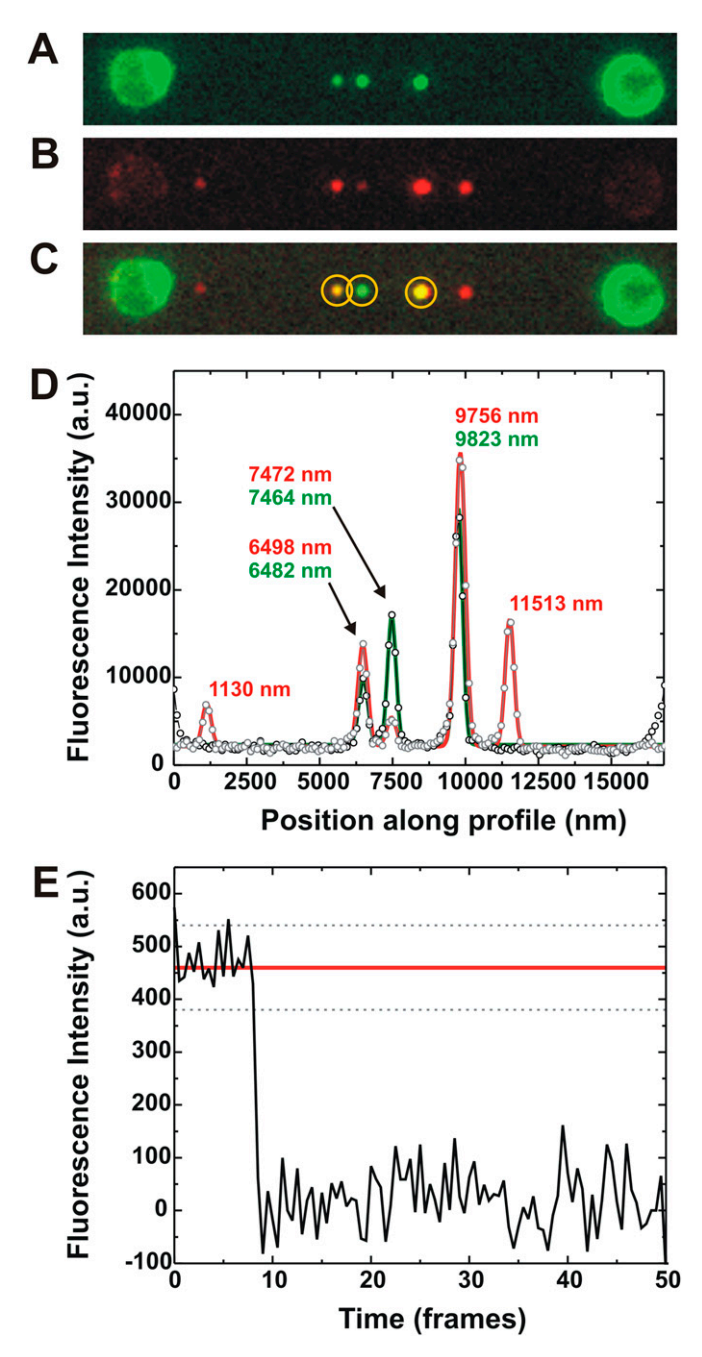


Fig. S6. RAD51 growth on dsDNA involves different RAD51 species, including monomers and preassembled oligomeric RAD51 complexes. (*A*) Integrated fluorescence image (sum of eight frames; contrast is graphically enhanced for clarity) of a lambda phage dsDNA molecule (48,502 bp; length, 16.4 μm) held at 40 pN after incubation with 75 nM RAD51 for 77 s. After visualization, continuous exposure resulted in complete photobleaching of all the fluorescent spots. (*B*) Integrated fluorescent image (eight frames; contrast is graphically enhanced for clarity) of the same dsDNA molecule reincubated with RAD51 for a second cycle of 77 s. We observed five fluorescent spots. (*C*) Overlaying *A* and *B* allows one to distinguish between growth and new nucleation events. In the yellow circles are examples of patch colocalization. (*D*) A line profile of the fluorescent intensity along the dsDNA is plotted. The line profile of *A* (black dots) shows three distinct peaks. Using a Gaussian fit (green), we found the center of the peaks at subpixel accuracy. The same process was repeated for *B*. The gray dots represent the line profile, whereas the red solid line is the outcome of the Gaussian fit. We found that in two cases, the colocalization of the patches was with sub–20-nm precision (6,498 nm vs. 6,482 nm and 7,472 nm vs. 7,464 nm). In the third case, we show that the actual distance between the two patches is 67 nm (9,756 nm vs. 9,823 nm). Note that the line profile is made by summing the intensity of eight image frames. (*E*) A photobleaching trace of the fluorescent spot at position 7,472 nm detected in the second incubation cycle (growth event) shows one individual step, in agreement with our single-molecule fluorescence calibration, and demonstrates in a direct way that extension of RAD51 may take place in the form of individual RAD51 monomers. The trace is obtained by integration of individual fluorescent spots in single image frames (i.e., the intensity is eight times lower than that of the profile *D*, which is obta

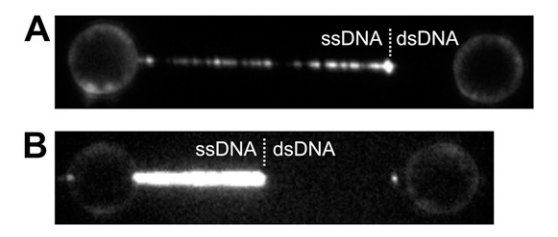


Fig. 57. Hybrid ss-dsDNA constructs reveal substrate specificity of human RAD51. These examples illustrate how the RAD51 filament formation rate is affected by the substrate. The measurements were taken at low force (F < 20 pN). To generate the hybrid templates, a lambda phage dsDNA molecule labeled with biotin on the ends of the same strand was held at the end-to-end distance of 22  $\mu$ m at 65 pN for  $\sim$ 60 s. We found that in cases in which an individual nick was present on the unlabeled strand of the DNA, a hybrid ss-dsDNA substrate was formed. Force—distance curves were taken to verify and quantify the extent of the ssDNA and dsDNA region. The incubation time in both cases was 60 s, and the RAD51 concentration was 75 nM. (A) Buffer used for the experiment was 20 mM Tris, pH 7.6; 100 mM KCl; 1 mM CaCl<sub>2</sub>; 0.5 mM ATP; and 10 mM DTT. (B) Buffer used for the experiment was 20 mM Tris, pH 7.6; 10 mM Mg(OAc)<sub>2</sub>; 2 mM CaCl<sub>2</sub>; 1 mM ATP; and 10 mM DTT (same as in ref. 1).

1. Carreira A, et al. (2009) The BRC repeats of BRCA2 modulate the DNA-binding selectivity of RAD51. Cell 136(6):1032-1043.

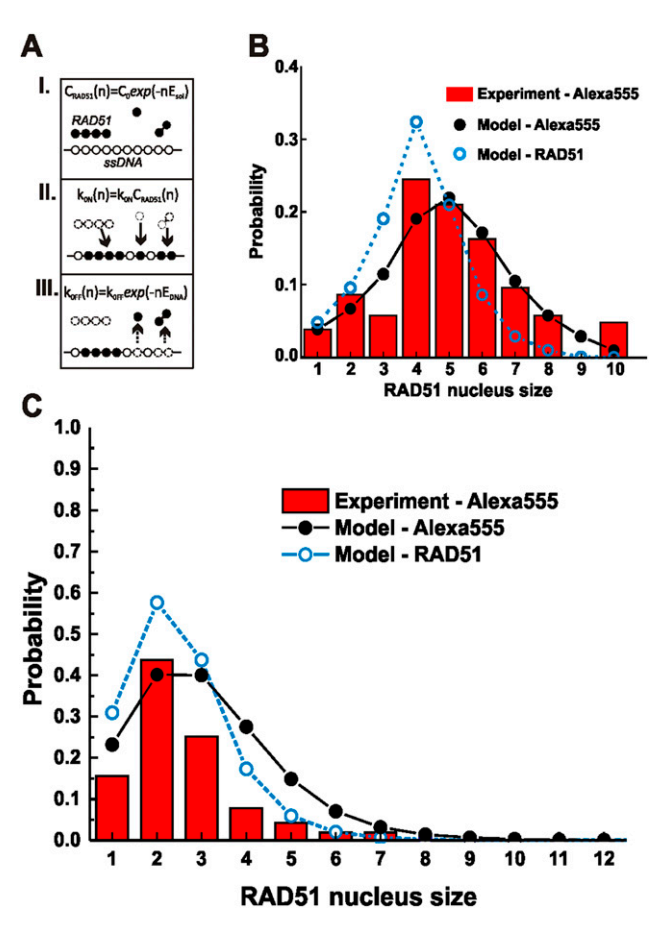


Fig. S8. Maximum-likelihood fitting of RAD51 filament formation of ssDNA. (A) A schematic representation of our kinetic model. In the model, assembly and disassembly are regulated by free energy parameters  $E_{sol}$  (related to the RAD51 monomer concentration in solution and the monomer—monomer dissociation constant through Eq. S1) and  $E_{DNA}$  (representing the contribution of each RAD51 monomer in a nucleus to the energy barrier of dissociation of the nucleus from ssDNA). (I) The single monomer—monomer interaction free energy of RAD51 in solution  $E_{sol}$  (results in an exponential decay of the concentration of RAD51 I-mers in solution for increasing oligomer size. (I) The on-rate (I) of a RAD51 I-mer binding to ssDNA is considered to be independent of I and dependent only on the concentration of the particular I-mer. (I) The off-rate (I) of a RAD51 I-mer detaching from ssDNA depends exponentially on I because of the equal free energy contribution (I) each monomer makes to the interaction of the I-meric nucleus with the DNA. (I) Probability of observing a certain nucleus size. Red bars, histogram of the number of fluorophores included in a RAD51 nucleus as obtained from wide-field fluorescence microscopy assays (same as Fig. 1I); black and line, optimal maximum-likelihood fit using the model from I; blue I0 and line, optimal maximum-likelihood fit where the number of fluorophores is transformed to the most likely number of RAD51 monomers, on the basis of the known fluorophore-to-RAD51 monomer ratio. For a more detailed description of the maximum-likelihood approach and results, see I1 I2 I3 I3. Shown are the histogram of the sizes of individual nuclei and a curve representing our stochastic model. Note that this is not a fit: the parameters obtained from the maximum-likelihood fit in I3 were used to calculate the distribution for the experimental conditions used in the real-time confocal experiments. In this modeling approach, an incubation time of 3 s was used,

Table S1. Growth probability as a function of RAD51 concentration

Growth probability

RAD51 concentration, nM	Growing nuclei, <i>n</i>	Total nuclei, <i>n</i>	Events per incubation	Events per second	Nucleation rate (nucleation per nt per second)	Kinetic cooperativity
7.5	6	83	0.07	$5.7 \times 10^{-4}$	$2.1 \times 10^{-7}$	2,700
12.5	2	32	0.06	$8.1 \times 10^{-4}$	$3.3 \times 10^{-7}$	2,450
25	8	81	0.10	$4.0 \times 10^{-3}$	$1.5 \times 10^{-6}$	2,670
50	13	244	0.05	$2.3 \times 10^{-3}$	$2.5 \times 10^{-6}$	920
75	32	68	0.471	$3.1 \times 10^{-2}$	$1.9 \times 10^{-5}$	1,630